2013

Long-period ocean sound waves constrain shallow slip and tsunamis in megathrust ruptures

Kozdon, Jeremy E.

Long-Period Ocean Sound Waves Constrain Shallow Slip and Tsunamis in Megathrust Ruptures

Jeremy E. Kozdon,[1*] Eric M. Dunham[2]

[1]Department of Applied Mathematics, Naval Postgraduate School,
833 Dyer Road, Monterey, CA 93943, USA
[2]Department of Geophysics and Institute for Computational and Mathematical Engineering,
Stanford University, 397 Panama Mall, Stanford, CA 94305, USA

[*]To whom correspondence should be addressed; E-mail: jekozdon@nps.edu.

Great earthquakes along subduction-zone plate boundaries, like the magnitude 9.0 Tohoku-Oki, Japan, event, deform the seafloor to generate massive tsunamis. Tsunami wave heights near shore are greatest when excitation occurs far offshore near the trench, where water depths are greatest and fault slip is shallow. Unfortunately the rupture process there is poorly constrained with land-based geodetic and even seafloor deformation measurements. Here we demonstrate, through dynamic rupture simulations of the Tohoku event, that long-period sound waves in the ocean, observable with ocean-bottom pressure sensors and/or seismometers, can resolve the shallow rupture process and tsunami excitation near the trench. These waves could potentially be used to improve local tsunami early warning systems.

Perhaps the most surprising aspect of the 2011 M_w 9.0 Tohoku-Oki, Japan, megathrust earthquake was the occurrence of extreme shallow slip, likely in excess of 30 m near the

trench (*1–5*). Shallow slip enhances seafloor uplift and increases tsunami wave heights, particularly when excitation occurs in the deepest part of the ocean near the trench. Rapid identification and quantification of shallow slip and near-trench seafloor uplift is of paramount importance for tsunami early warning systems. This is particularly true in the near-field, where coastal communities have only $\sim$10–30 minutes before the arrival of the leading wave. In many subduction zones, including the Japan Trench, resolution of the near-trench region $\sim$100–200 km offshore is effectively impossible with land-based geodetic data (*6, 7*). On the other hand, the complexity of the seismic wavefield makes it challenging to uniquely constrain the spatial distribution of slip, leading to uncertainty in predicted tsunami amplitudes.

Here we describe how long-period sound waves in the ocean can be used to quantify the amount of shallow slip, seafloor uplift, and tsunami excitation in megathrust events. Of particular interest are PL waves, which have periods of a few seconds and propagate from the trench toward the coast at about 6 km/s. PL waves are multiply reflected sound waves partially trapped in the ocean but penetrating into the underlying solid Earth as evanescent compressional waves and radiating shear waves (*8–10*). PL waves are quite distinct from the much higher frequency ($>$ 2 Hz) T waves, which are purely acoustic modes trapped within the low-velocity SOFAR channel (*11, 12*). As we demonstrate, PL-wave amplitudes correlate well with near-trench seafloor uplift, as do those of acoustic organ-pipe modes in the ocean directly above the trench. Because of their large amplitudes and long periods, both types of waves should be easily detectable with cabled ocean-bottom pressure sensor and/or seismometer networks of the type currently being deployed offshore Japan and in other subduction zones (*13*), and possibly used to improve local tsunami early warning systems.

We identified the link between these long-period sound waves and tsunami excitation through dynamic rupture simulations of the Tohoku earthquake (*14*). Dynamic rupture simulations take as inputs the stresses acting on the fault just prior to rupture, and simultaneously solve for the

slip history and seismic and acoustic wavefields that are consistent with the fault friction law and the momentum balance and material response of the solid Earth and overlying compressible ocean. We use a rate-and-state friction law in which fault shear strength evolves, over a characteristic slip distance, toward a steady state strength that is either an increasing or decreasing function of fault slip velocity (*15*). These behaviors are known as velocity-strengthening and velocity-weakening, respectively; the latter is necessary for unstable slip and earthquake nucleation while the former is usually associated with aseismic sliding. We additionally account for buffering of effective normal stress changes by poroelastic fault-zone effects. We initially developed these simulations to study how frictional properties along the shallowest portion of the plate interface influence the ability of ruptures to reach the trench, finding that surface-breaking rupture is possible even through >30-km-long velocity-strengthening segments (*14*).

Because the Tohoku rupture extended nearly 500 km along strike and only 200 km down-dip we neglect variations in the along-strike direction. This renders the model two-dimensional, and allows us to focus on the along-dip rupture process and wave propagation toward and away from the coast. We perform high-resolution simulations using a provably stable and accurate multiblock finite-difference method (*16*), with a realistic structural model (*17*) (Fig. 1A and Table S1). The progression of the rupture and evolution of the wavefield from one of our simulations are shown in movie S1 and the remaining panels of Fig. 1. After nucleating about 100 km offshore, the rupture grows bilaterally. Down-dip propagation ceases around the coastline due to a change in frictional properties. The rupture continues up-dip, eventually reaching the trench and exciting a large burst of seismic and acoustic waves. Most prominent are ≈14-s oceanic Rayleigh waves channeled offshore within the ocean and underlying oceanic crust, which produce >1-MPa acoustic pressure changes in the ocean. In addition, there are large-amplitude acoustic reverberations, or organ-pipe modes, above the trench. PL waves and acoustic waves returning toward the coast are also evident; we will shortly investigate these in greater detail but

first we discuss the rupture process.

Fig. 2A shows the slip history from four simulations representing a wide range of possible frictional properties near the trench (Table S2 and Fig. S1); the deeper section of the fault is velocity-weakening and always slips unstably. In each case the average stress drop was tuned, by varying the initial effective normal stress on the fault, to match both onshore 1-Hz GPS displacements (Fig. 2B) and static seafloor deformation data (Fig. 2C and D). With the exception of the seafloor measurements closest to the trench (*3*), which are subject to large uncertainties, these data cannot be used to distinguish between the various models.

While the four models have nearly identical slip profiles at depth, they differ substantially over the final $\sim$50 km near the trench. These differences in shallow slip influence tsunami excitation, as illustrated in Fig. 2E through the predicted sea surface uplift immediately following the earthquake. Our simulations currently neglect gravitational restoring forces and thus these predictions are simply estimates employing several assumptions (instantaneous uplift of an incompressible, hydrostatic ocean, due to both vertical seafloor uplift and horizontal advection of bathymetric slopes (*18*)). It is essential, for local tsunami early warning systems, to be able to rapidly distinguish between these different models. This can be most accurately accomplished by directly measuring the effectively hydrostatic pressure changes on the seafloor beneath the tsunami itself. But due to the slow propagation speed of tsunamis ($\sim$100 m/s), with this approach only instruments nearly 200 km offshore could be used to distinguish between these different models in the first few minutes after the earthquake. Pressure sensors close to shore would not detect tsunami waves from the near-trench region until nearly ten minutes later.

Our simulations suggest a potential use for instruments closer to shore during the time prior to tsunami wave arrivals, namely using long-period sound waves to rapidly constrain near-trench seafloor motions and tsunami excitation. PL waves are evident in wavefield snapshots (Fig. 1B-D and movie S1) and space-time plots of fields on the seafloor (Figs. 3 and S2–S4) as $\sim$1-MPa

oscillations at periods of several seconds that propagate toward the coast at about 6 km/s. Particle motions on the seafloor are prograde elliptical, a distinctive feature of PL waves (*8, 9*). The PL waves can be identified out to distances of about 175 km from the coast, beyond which interference with other waves excited near the trench by the propagating rupture overly complicates the waveforms. Later arrivals labeled as acoustic modes in Fig. 3 have shorter periods and travel closer to the sound speed in the ocean. Accurate prediction of these waves requires accounting for the low-velocity SOFAR channel, especially at frequencies $>$1 Hz where these arrivals would include T waves.

We next examine pressure and velocity seismograms at several seafloor locations (Figs. 4 and S5–S8). The PL wave amplitudes correlate well with near-trench seafloor uplift (Fig. 1c) and, unlike onshore 1-Hz GPS displacements, could thus be used to distinguish between the different models. PL waves could be measured with pressure sensors (especially on or near the seafloor where amplitudes are largest), ocean-bottom seismometers, and possibly even SOFAR-channel hydrophones (like those in the International Monitoring System (*19*)). Wave amplitudes are remarkably large; in fact, predicted pressure changes in our Tohoku simulations are $\sim$1 MPa over most of the seafloor, making this signal two orders of magnitude larger than the $\sim$10-kPa hydrostatic pressure changes associated with the passage of $\sim$1-m-high tsunami waves. These sound waves should therefore be easily detectable with ocean-bottom pressure sensors sampling at 1–10 Hz or faster; it is likely that they were recorded at stations TM1 and TM2 during the Tohoku event (*20, 21*), though that data is not presently available to test our predictions.

Another potentially valuable part of the wavefield for tsunami warning and earthquake source studies is the fundamental organ-pipe mode excited above the trench (Figs. 3 and S2–S4). This mode is comprised of vertically propagating sound waves that bounce between the seafloor and sea surface with characteristic period $4H/c_f \approx 14$ s, where H is the ocean depth and c_f is the fluid sound speed (*22*). This mode has vertical wavelength $\approx 4H$ and a temporal quality

factor exceeding ten due to the high impedance contrast between the ocean and solid Earth (*10*). The wave amplitude correlates well with seafloor uplift, as noted previously for the 2003 M_w 8.3 Tokachi-Oki, Japan, earthquake using pressure sensors offshore Hokkaido (*23, 24*).

The largest amplitude waves (Figs. 3 and S2–S4) travel along with the propagating rupture before continuing offshore; thus they initially have phase velocities faster than the ocean sound speed and are strongly enhanced by offshore directivity. These oceanic Rayleigh waves continue propagating seaward with a group velocity, at $\sim$10 s period, somewhat higher than the ocean sound speed (*25–27*). In contrast to the PL waves, the oceanic Rayleigh wave amplitudes are quite similar in all models and are determined by the overall moment release along the entire seismogenic zone. While they would therefore be of no use in elucidating the near-trench rupture process, these waves could easily be detected and potentially used in slip inversions.

As shown here, various types of long-period ocean sound waves can be used to constrain important details of the megathrust rupture process and tsunami excitation. Our simulations suggest how local tsunami early warning systems based on an offshore sensor network might be improved by incorporating additional data associated with acoustic and seismic waves. And, at the very least, records of these waves from the Tohoku event (*20, 21*) will permit us to distinguish between the various rupture models presented in this work. Additionally, because these waves are likely sensitive to the time scale over which the seafloor deforms, they might allow us to determine if shallow slip accumulated over several minutes, as in so-called tsunami earthquakes (*28*), or rapidly as in our model. With only a minor change to the traction-free boundary condition on ocean surface, our simulations can be extended to include gravitational restoring forces, giving us the ability to simulate not only seismic and acoustic waves, but also tsunamis.

References and Notes

1. M. Sato, *et al.*, *Science* **332** (2011).

2. S. Ide, A. Baltay, G. C. Beroza, *Science* **332**, 1426 (2011).

3. Y. Ito, *et al.*, *Geophys. Res. Lett.* **38** (2011).

4. M. Kido, Y. Osada, H. Fujimoto, R. Hino, Y. Ito, *Geophys. Res. Lett.* **38** (2011).

5. T. Fujiwara, *et al.*, *Science* **334** (2011).

6. J. P. Loveless, B. J. Meade, *J. Geophys. Res.* **115** (2010).

7. S. Miyazaki, J. J. McGuire, P. Segall, *Earth Planets Space* **63**, 637 (2011).

8. J. Oliver, M. Major, *Bull. Seismol. Soc. Am.* **50**, 165 (1960).

9. R. A. Phinney, *J. Geophys. Res.* **66**, 1445 (1961).

10. R. A. W. Haddon, *Bull. Seismol. Soc. Am.* **77**, 1804 (1987).

11. M. Ewing, I. Tolstoy, F. Press, *Bull. Seismol. Soc. Am.* **40**, 53 (1950).

12. E. A. Okal, P.-J. Alasset, O. Hyvernaud, F. Schindelé, *Geophys. J. Int.* **152**, 416 (2003).

13. R. Monastersky, *Nature* **483**, 144 (2012).

14. J. E. Kozdon, E. M. Dunham, *Bull. Seism. Soc. Am.* **103**, 1275 (2013).

15. J. R. Rice, N. Lapusta, K. Ranjith, *J. Mech. Phys. Solids* **49**, 1865 (2001).

16. J. E. Kozdon, E. M. Dunham, J. Nordström, *J. Sci. Comp.* **55**, 92 (2013).

17. S. Miura, *et al.*, *Earth Planet. Sci. Lett.* **407**, 165 (2005).

18. Y. Tanioka, K. Satake, *Geophys. Res. Lett.* **23**, 861 (1996).

19. S. Yildiz, K. Sabra, L. M. Dorman, W. A. Kuperman, *Geophys. Res. Lett.* **40**, 1 (2013).

20. T. Maeda, T. Furumura, S. Sakai, M. Shinohara, *Earth Planets Space* **63**, 803 (2011).

21. H. Tsushima, *et al.*, *Earth Planets Space* **63**, 821 (2011).

22. H. Miyoshi, *J. Oceanogr. Soc. Japan* **10**, 1 (1954).

23. M. A. Nosov, S. V. Kolesov, *Nat. Hazards Earth Syst. Sci.* **7**, 243 (2007).

24. F. Chierici, L. Pignagnoli, D. Embriaco, *J. Geophys. Res.* **115** (2010).

25. M. A. Biot, *Bull. Seism. Soc. Am.* **42**, 81 (1952).

26. T. Yamashita, R. Sato, *J. Phys. Earth* **24**, 397 (1976).

27. E. Eyov, A. Klar, U. Kadri, M. Stiassnie, *Wave Motion* **50**, 929 (2013).

28. H. Kanamori, *Phys. Earth Planet. Interior.* **6**, 346 (1972).

29. S. Ozawa, *et al.*, *Nature* **475**, 373 (2011).

Acknowledgments: This work was supported by the National Science Foundation (OCI-1122734 to JEK, EAR-1255439 to EMD) and the Alfred P. Sloan Foundation (BR2012-097 to EMD). We thank Shin'ichi Miyazaki for providing the GEONET data.

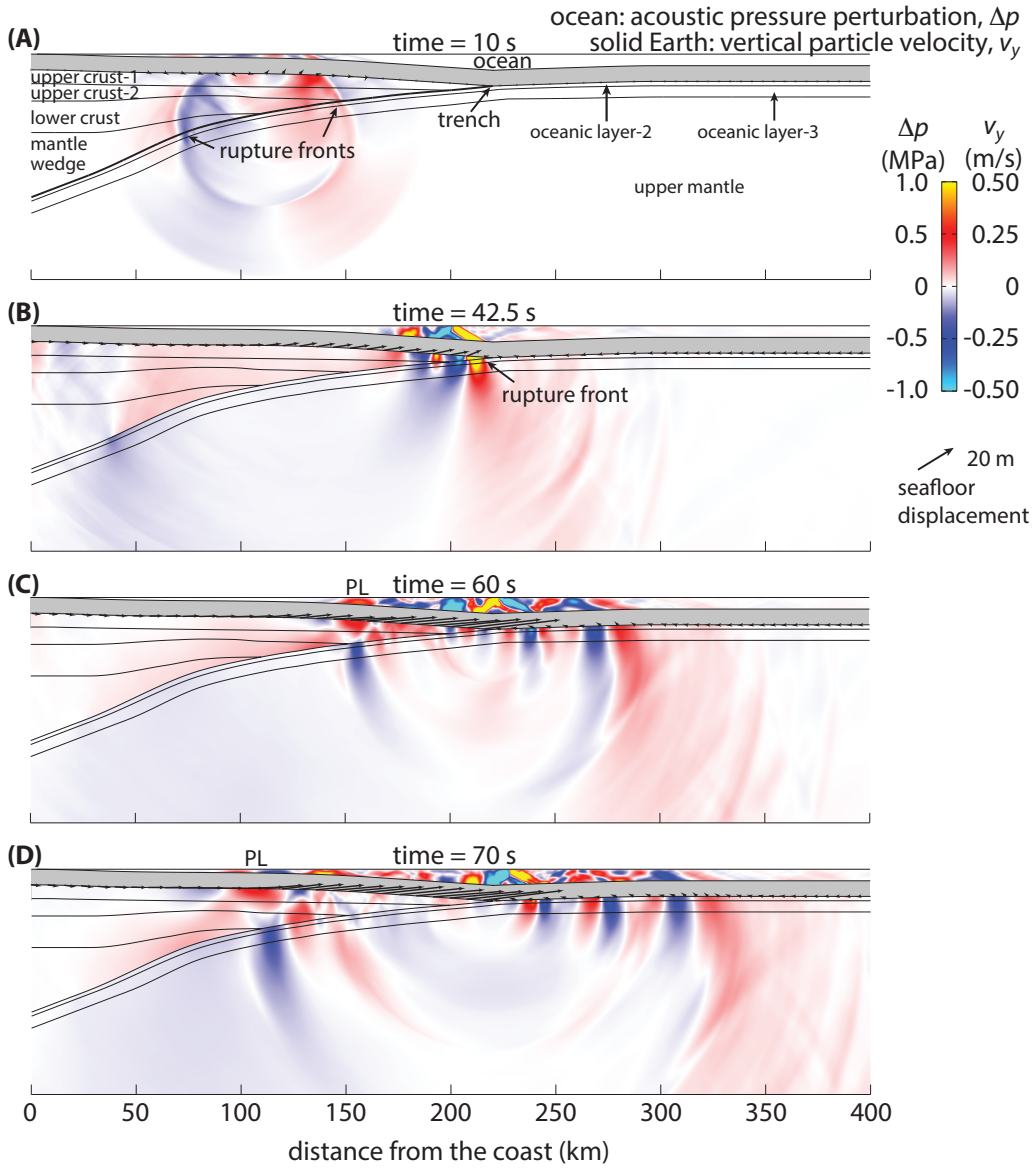

Fig. 1. Seismic and acoustic wavefield from 2011 Tohoku-Oki dynamic rupture simulation. Wavefield snapshots from our simulation of the 2011 Tohoku earthquake with velocity-weakening friction everywhere along the plate interface. (**A**) Bilateral rupture growth, with hypocentral P and S waves and early reflections visible. (**B**) Rupture reaches trench; note multiply reflected sound waves in ocean propagating at supersonic horizontal velocity. (**C**) and (**D**) Oceanic Rayleigh waves propagate offshore; PL waves propagate landward.

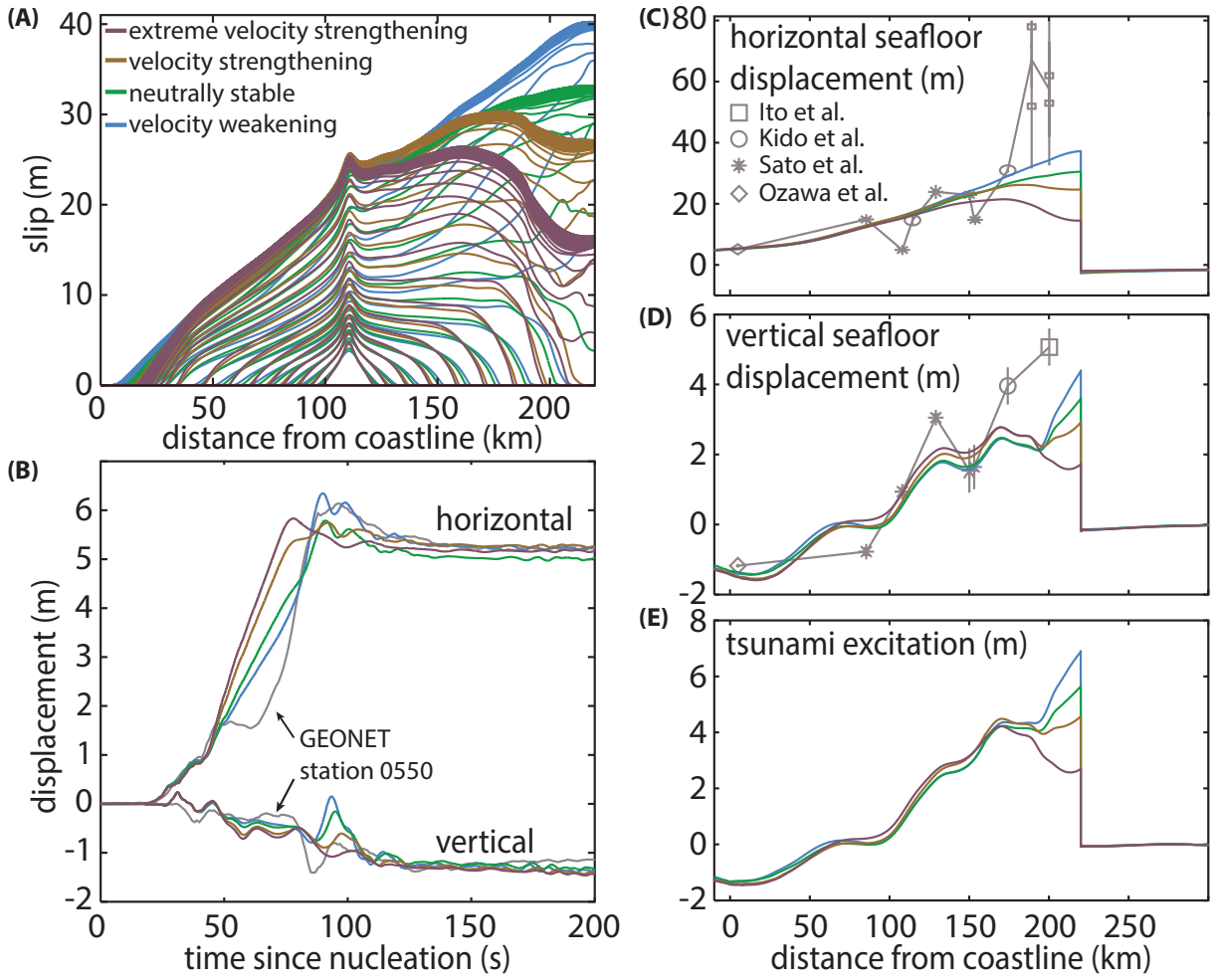

Fig. 2. Model predictions and data for 2011 Tohoku-Oki earthquake. (**A**) Slip histories from simulations employing a range of possible frictional properties near the trench. Also shown are comparisons of model predictions with (**B**) 1-Hz GPS displacements recorded at the coast (GEONET station 0550 operated by the Geospatial Information Authority of Japan) and (**C** and **D**) static seafloor deformation measurements (*1, 3, 4, 29*). (**E**) Predicted tsunami excitation, shown as initial sea surface elevation assuming instantaneous response of an incompressible, hydrostatic ocean. The models differ substantially near the trench, but this region cannot be resolved with land-based geodetic data.

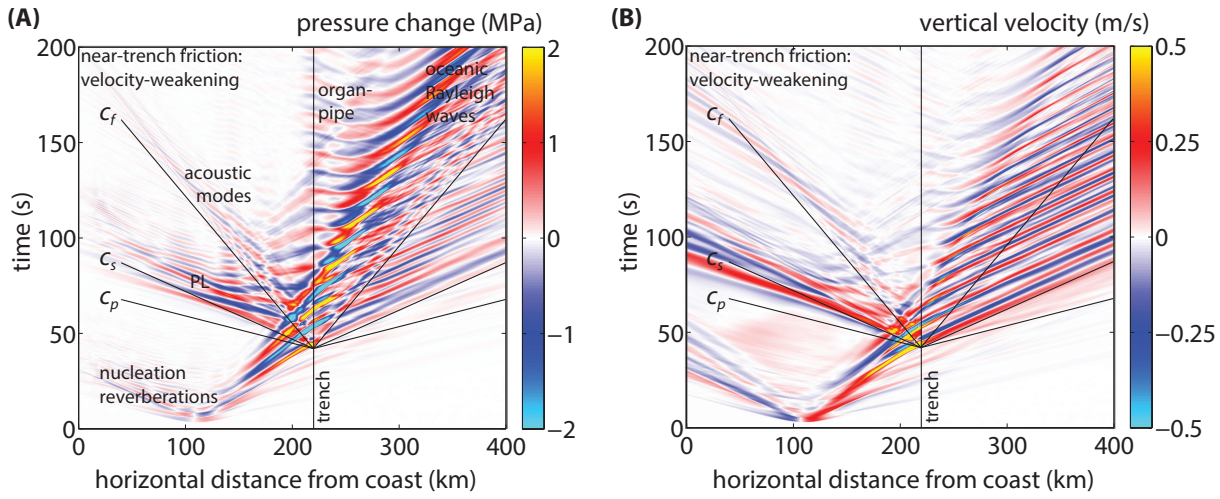

Fig. 3. Seismic and ocean acoustic wavefields on the seafloor. Space-time plots of (**A**) pressure change and (**B**) vertical particle velocity on the seafloor. Lines show wave speeds: $c_f = 1.5$ km/s (ocean sound speed), $c_p = 7$ km/s and $c_s = 4$ km/s (lower crust P- and S-wave speeds). PL waves traveling from the trench toward shore at 6 km/s and organ-pipe reverberations above the trench have amplitudes that correlate with the shallow slip and near-trench seafloor uplift. Large-amplitude oceanic Rayleigh waves propagate offshore at group velocities slightly less than the ocean sound speed. Shown for the velocity-weakening case.

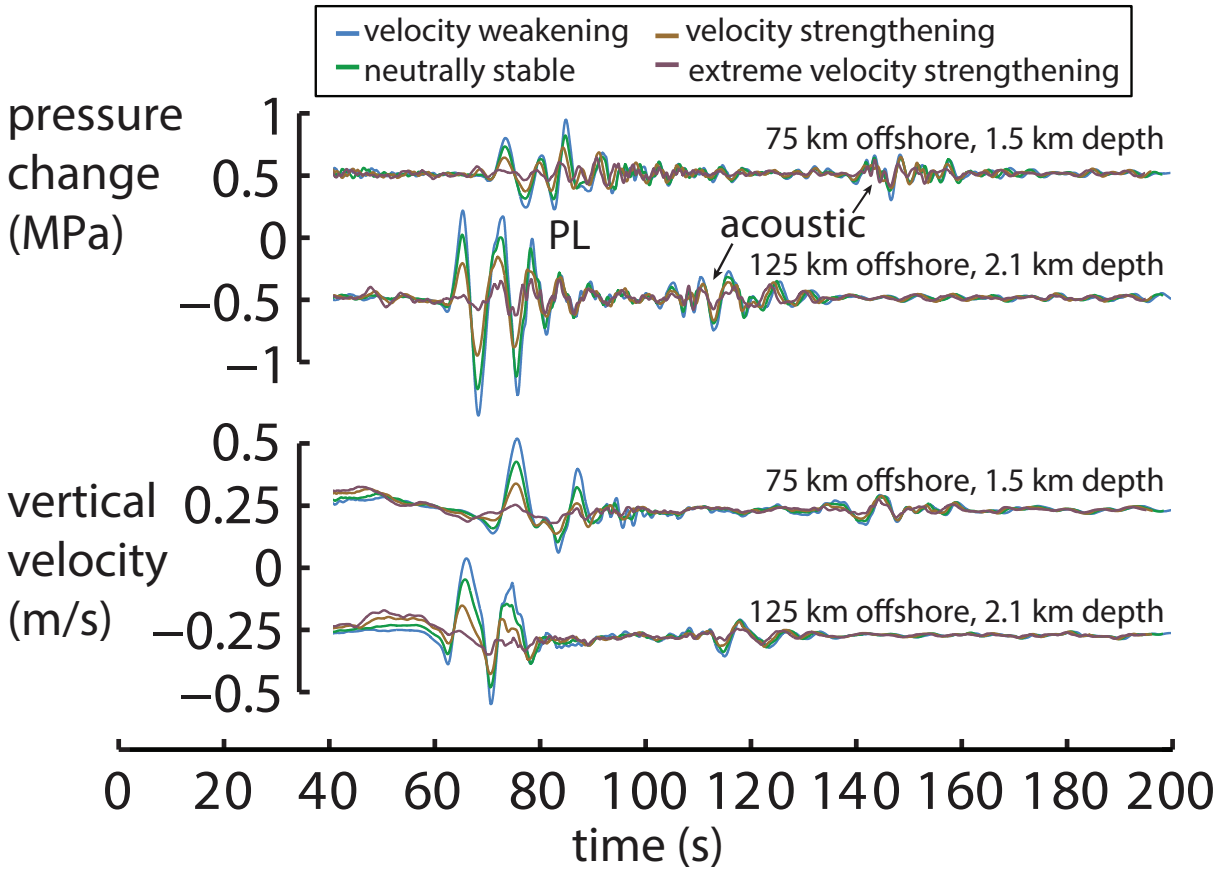

Fig. 4. Synthetic seismograms and pressure changes at seafloor stations. Acoustic pressure perturbations in the ocean and vertical particle velocities in the solid Earth at various points along the seafloor for the models shown in Fig. 2, which differ only near the trench. PL waves are sensitive to these differences.

Supplementary Material for Long-Period Ocean Sound Waves Constrain Shallow Slip and Tsunamis in Megathrust Ruptures

Jeremy E. Kozdon,* Eric M. Dunham

*To whom correspondence should be addressed; E-mail: jekozdon@nps.edu.

Materials and Methods

In our dynamic rupture simulations we simultaneously solve for the seismic and acoustic wavefields and the slip history on the fault. The method and model parameters are largely the same as those in the simulations of Kozdon and Dunham (*1*), but with improvements to the structural model (especially bathymetry). Also, in contrast to our previous study, all simulations now have an ocean layer.

We summarize the methodology here. The solid Earth response is linear elastic and the ocean is treated as a linear acoustic medium. We neglect gravitational restoring forces in the momentum balance, except in setting the initial tractions on the fault surface as described subsequently. The geometry and off-fault material properties are based on the structural model of Miura et al. (*2*), though with a smoother bathymetry than in our original simulations (*1*). The new bathymetry averages over along-strike bathymetric variations to provide a more representative two-dimensional profile. The material properties are piecewise constant with values given in Table S1.

The fault obeys the rate-and-state friction law (*1, 3, 4*)

$$\frac{d\tau}{dt} = \frac{a\bar{\sigma}}{V} \tanh\left(\frac{\tau}{a\bar{\sigma}}\right) \frac{dV}{dt} - \frac{V}{L}\left[|\tau| - \bar{\sigma} f_{ss}\left(V\right)\right], \tag{1}$$

with steady state friction coefficient

$$f_{ss}(V) = f_0 - (b-a)\ln(V/V_0), \tag{2}$$

in which τ is the shear strength of the fault, V is the slip velocity, $\bar{\sigma}$ is the effective normal stress, a and b are dimensionless rate-and-state friction parameters, L is the state evolution distance, and f_0 is the friction coefficient for steady sliding at reference velocity V_0. The sign of $b-a$ determines if steady state frictional strength decreases ($b-a>0$, velocity-weakening) or increases ($b-a<0$, velocity-strengthening) with increasing slip velocity. With this form of the friction law, shear strength does not respond instantaneously to abrupt changes in effective normal stress. This is particularly important to avoid ill-posedness that can arise in bimaterial sliding problems for friction laws in which τ is directly proportional to the instantaneous value of $\bar{\sigma}$ (*4, 5*).

Some frictional properties are spatially uniform ($f_0 = 0.6$, $V_0 = 1$ μm/s, and $L = 0.8$ m), while others (a and b) vary with depth. Over most of the fault, $a = 0.016$ and $b = 0.02$ such that $b-a = 0.004$ and fault slip is unstable. To control the down-dip extent of rupture, we increase a such that $b-a$ becomes negative (velocity-strengthening) below about 40 km depth (Fig. S1A). That depth is chosen to match vertical seafloor displacement and onshore displacement data (*1*).

We present four models that have differing friction properties, and hence rupture behavior, in the near-trench region. Specifically, we vary b (while retaining $a = 0.016$) along the upper part of the fault, extending 30 km horizontally from the trench, as given in Supplementary Table 2. These four models also differ in terms of initial stress conditions as described below, but are otherwise identical.

We account for undrained poroelastic alterations of fault-zone pore pressure, Δp, in response to changes in total normal stress, $\Delta\sigma$, using a linear relation of the form $\Delta p = B\Delta\sigma$, where $B = 0.6$. Thus,

$$\bar{\sigma} = \bar{\sigma}_0 + (1 - B)\Delta\sigma, \tag{3}$$

where $\bar{\sigma}_0$ is the initial effective normal stress on the fault prior to the rupture. Poroelastic effects thus partially buffer slip-induced changes in normal stress that occur on dipping faults and on faults juxtaposing dissimilar elastic solids; both effects occur in our simulations. This simple poroelastic model emerges as a limiting case of a more rigorous model (*6*) when the fault is bordered by highly damaged material; in that case, B is Skempton's coefficient.

We set initial effective normal stress on the upper section of the fault as the difference between lithostatic total normal stress and hydrostatic pore pressure. Below a certain depth we assume that pore pressure begins to track the lithostatic gradient, thus saturating $\bar{\sigma}_0$ at a constant value $\bar{\sigma}_{\max}$ below that depth (Fig. S1B). The maximum effective stress $\bar{\sigma}_{\max}$ (and the corresponding depth) are tunable model parameters that we select, in each of our four models, to obtain a reasonable fit to the onshore and offshore displacements (Table S2). The resulting final slip profiles are nearly identical between the four models at depth, but differ near the trench. This reflects a trade-off between average stress drop at depth, which increases with increasing $\bar{\sigma}_{\max}$, and effective length of the seismogenic zone, which decreases as the upper part of the fault becomes more velocity-strengthening.

The initial shear stress on the fault is set to $0.6\bar{\sigma}_0$. With the specific form of the rate-and-state law we use, we must also set the initial slip velocity V_{ini}. This is equivalent to setting the initial state variable in standard forms of rate-and-state friction; both approximately determine the peak strength of the fault (*7*). We use $V_{ini} = 1$ μm/s. Ruptures are nucleated by rapidly increasing shear stress over a small section of the fault at the desired hypocentral location, following the procedure in Kozdon et al. (*1*).

The combined system of equations are solved using the numerical method developed by Kozdon et al. (*8, 9*). The wave equations governing the elastic solid and acoustic fluid layers are solved using a multiblock finite difference method. The domain is divided into 42 four-sided blocks, potentially with curvilinear boundaries, separated by 71 interfaces. All material interfaces, and the fault, coincide with one or more of these computational interfaces. Normal and shear tractions are balanced across solid-solid interfaces, while only normal tractions are balanced across fluid-solid interfaces (at which shear tractions vanish). Each block is mapped to a rectangle in the computational domain and high-order summation-by-parts finite-difference operators are used to discretize the equations in the transformed coordinate system. The fundamental unknown fields in the medium are the stress changes and particle velocities, which are defined at all grid points and time steps (in contrast to staggered-grid finite-difference methods). An acoustic medium is obtained as a limiting case of an elastic medium by taking shear modulus (and hence shear-wave speed) to zero. Interface conditions, including the nonlinear fault friction law, are enforced weakly using penalty terms added to the semi-discrete system of equations. The overall method is provably stable and accurate.

Additional Results

Fig. 3 shows space-time plots of pressure changes and vertical velocity for the velocity-weakening simulation. Here we provide identical plots for the neutrally stable (Fig. S2), velocity-strengthening (Fig. S3), and extreme velocity-strengthening (Fig. S4) simulations.

Fig. 4 shows pressure and vertical velocity seismograms at two seafloor locations. Similar plots for additional seafloor locations are provided in Figs. S5–S8. Note that the amplitude of PL waves observed at stations landward of the trench increases with increasing shallow slip (Figs. S5 and S6). No such relation exists for the oceanic Rayleigh waves that are evident at stations seaward of the trench (Figs. S7 and S8). All simulations have comparable amplitudes

for the oceanic Rayleigh waves. This is likely because these waves are continuously excited as the rupture is propagating up-dip, making their amplitudes far less sensitive to the details of the shallow slip process and more determined by the overall rate of moment release along the entire extent of the fault.

References and Notes

1. J. E. Kozdon, E. M. Dunham, *Bull. Seism. Soc. Am.* **103**, 1275 (2013).

2. S. Miura, *et al.*, *Earth Planet. Sci. Lett.* **407**, 165 (2005).

3. J. R. Rice, *Pure Appl. Geophys.* **121**, 443 (1983).

4. J. R. Rice, N. Lapusta, K. Ranjith, *J. Mech. Phys. Solids* **49**, 1865 (2001).

5. K. Ranjith, J. R. Rice, *J. Mech. Phys. Solids* **49**, 341 (2001).

6. M. Cocco, J. R. Rice, *J. Geophys. Res.* **107**, ESE 2 (2002).

7. E. M. Dunham, D. Belanger, L. Cong, J. E. Kozdon, *Bull. Seism. Soc. Am.* **101**, 2296 (2011).

8. J. E. Kozdon, E. M. Dunham, J. Nordström, *J. Sci. Comp.* **50**, 341 (2011).

9. J. E. Kozdon, E. M. Dunham, J. Nordström, *J. Sci. Comp.* **55**, 92 (2013).

Layer Name	P-wave speed (km/s)	S-wave speed (km/s)	density (kg/m^3)
ocean	1.5	0	1000
upper crust-1	4.8	2.8	2200
upper crust-2	5.5	3.2	2600
lower crust	7.0	4.0	2800
mantle wedge	8.0	4.6	3200
oceanic layer-2	5.5	3.2	2600
oceanic layer-3	6.8	3.9	2800
uppermost mantle	8.0	4.6	3200

Table S1. Material properties. Density and wave speeds for material layers shown in Fig. 1.

Simulation name	$b-a$	$\bar{\sigma}_{\max}$ (MPa)
velocity-weakening	0.004	25
neutrally stable	0	30
velocity-strengthening	-0.004	40
extreme velocity-strengthening	-0.008	45

Table S2. Friction and stresses for all four simulations. Near-trench frictional parameter $b-a$ and maximum effective normal stress $\bar{\sigma}_{\max}$ at depth.

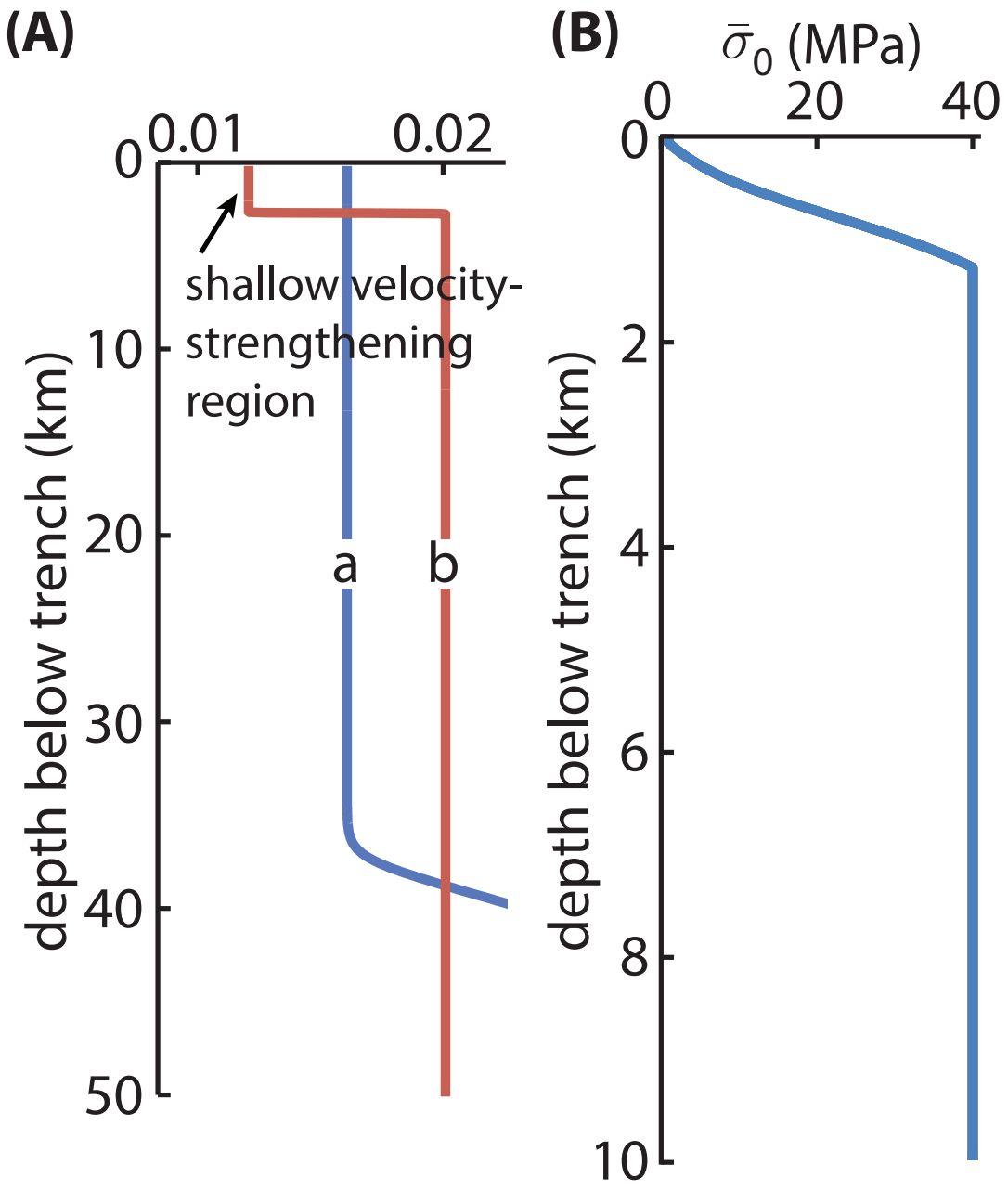

Fig. S1. Depth-dependence of friction and stress. Shown for near-trench velocity-strengthening model. (**A**) Rate-and-state parameters a and b. Regions with $b - a > 0$ are velocity-weakening. (**B**) Initial effective normal stress on the fault, $\bar{\sigma}_0$, with $\bar{\sigma}_{\max} = 40$ MPa.

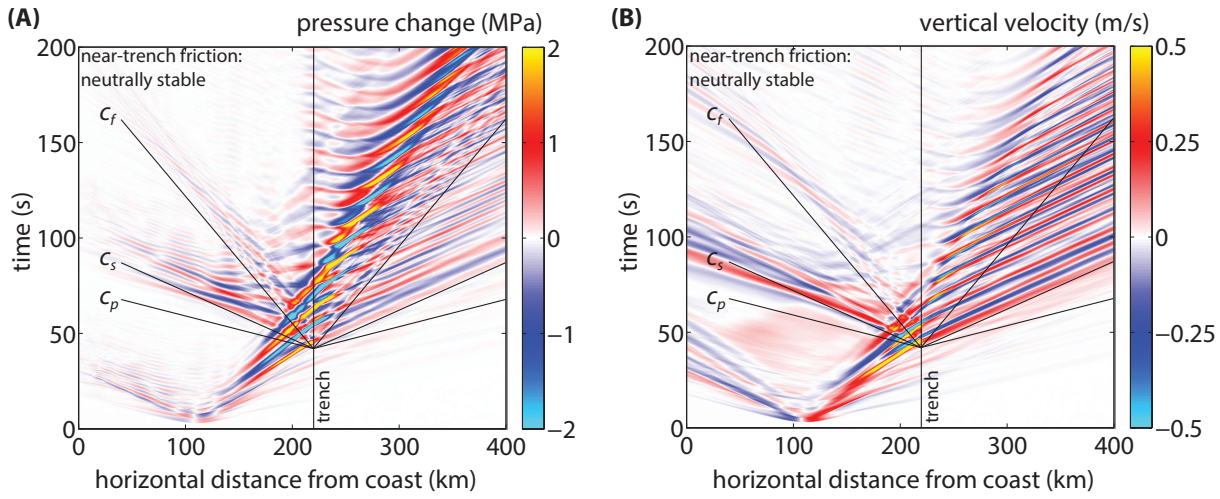

Fig. S2. Seismic and ocean acoustic wavefields on the seafloor. Space-time plots of (**A**) pressure change and (**B**) vertical particle velocity on the seafloor. Lines show wave speeds: $c_f = 1.5$ km/s (ocean sound speed), $c_p = 7$ km/s and $c_s = 4$ km/s (lower crust P- and S-wave speeds). Shown for the neutrally stable case.

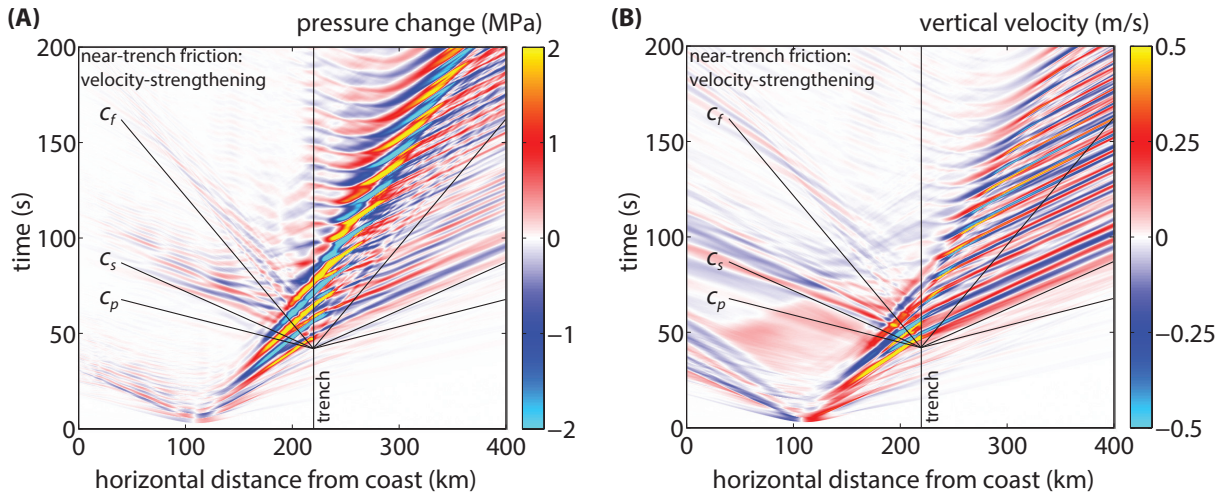

Fig. S3. Seismic and ocean acoustic wavefields on the seafloor. Space-time plots of (**A**) pressure change and (**B**) vertical particle velocity on the seafloor. Lines show wave speeds: $c_f = 1.5$ km/s (ocean sound speed), $c_p = 7$ km/s and $c_s = 4$ km/s (lower crust P- and S-wave speeds). Shown for the velocity-strengthening case.

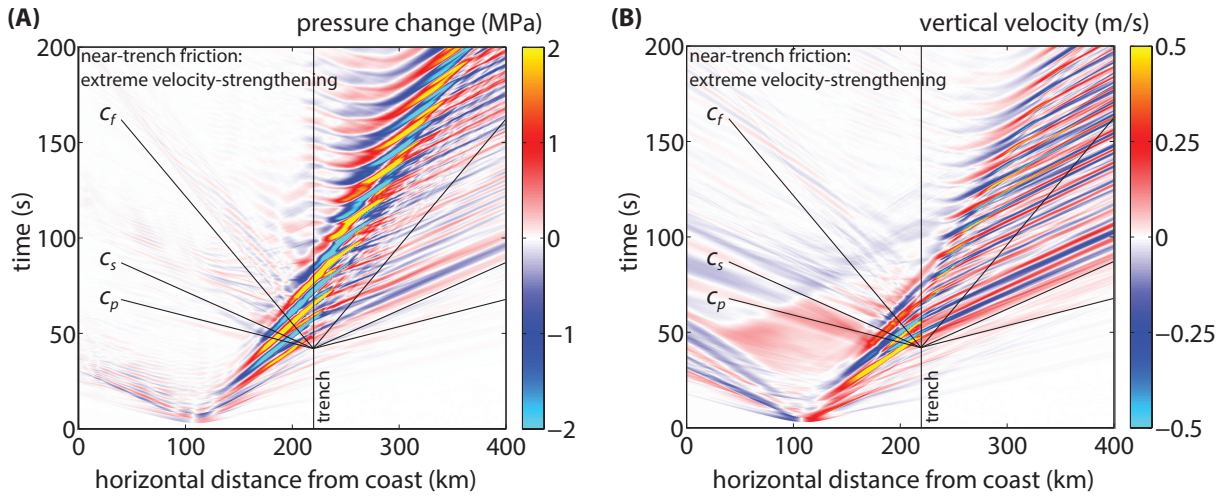

Fig. S4. Seismic and ocean acoustic wavefields on the seafloor. Space-time plots of (**A**) pressure change and (**B**) vertical particle velocity on the seafloor. Lines show wave speeds: $c_f = 1.5$ km/s (ocean sound speed), $c_p = 7$ km/s and $c_s = 4$ km/s (lower crust P- and S-wave speeds). Shown for the extreme velocity-strengthening case.

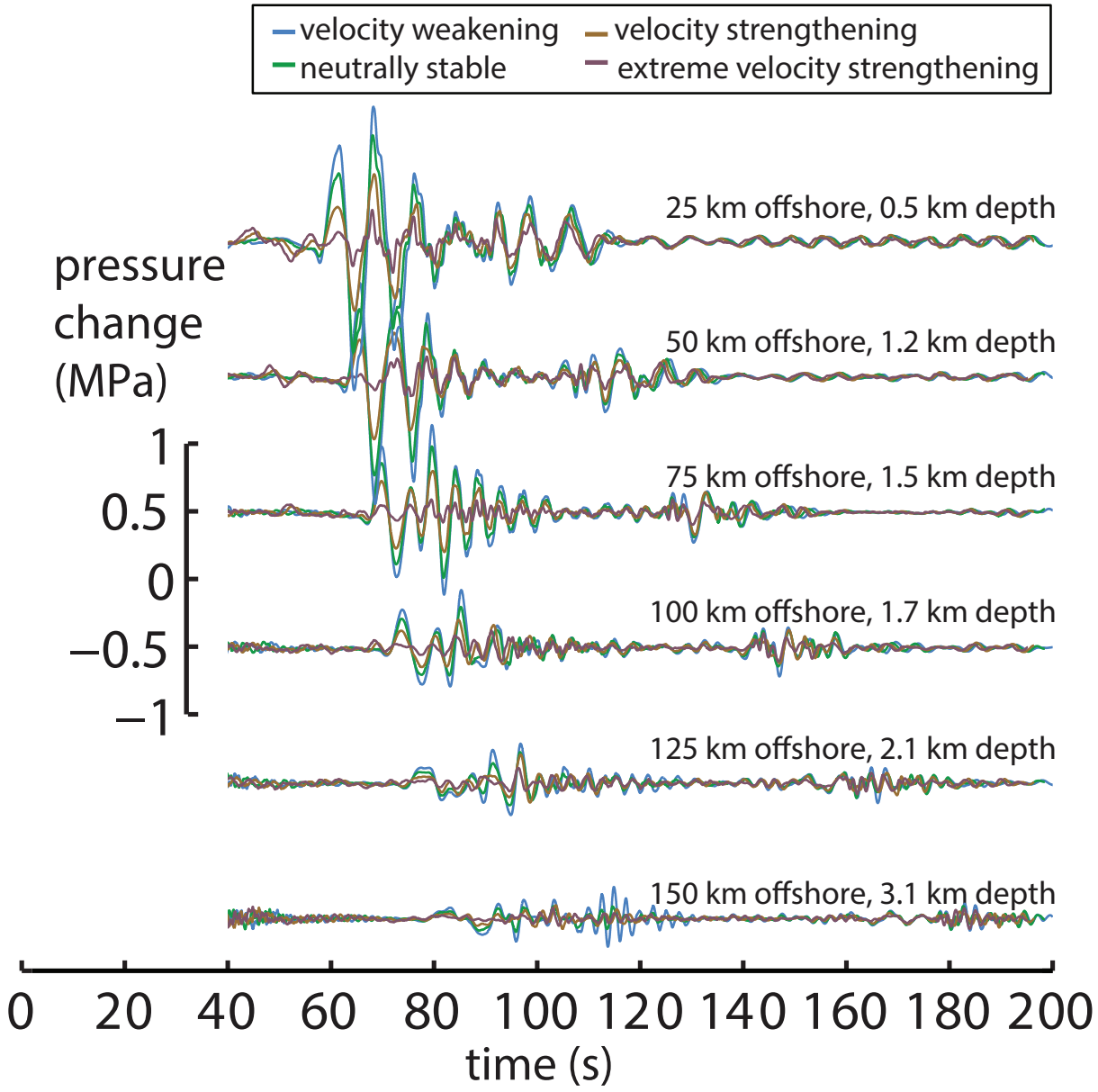

Fig. S5. Pressure changes at seafloor stations landward of trench. Acoustic pressure perturbations on the ocean bottom, landward of the trench.

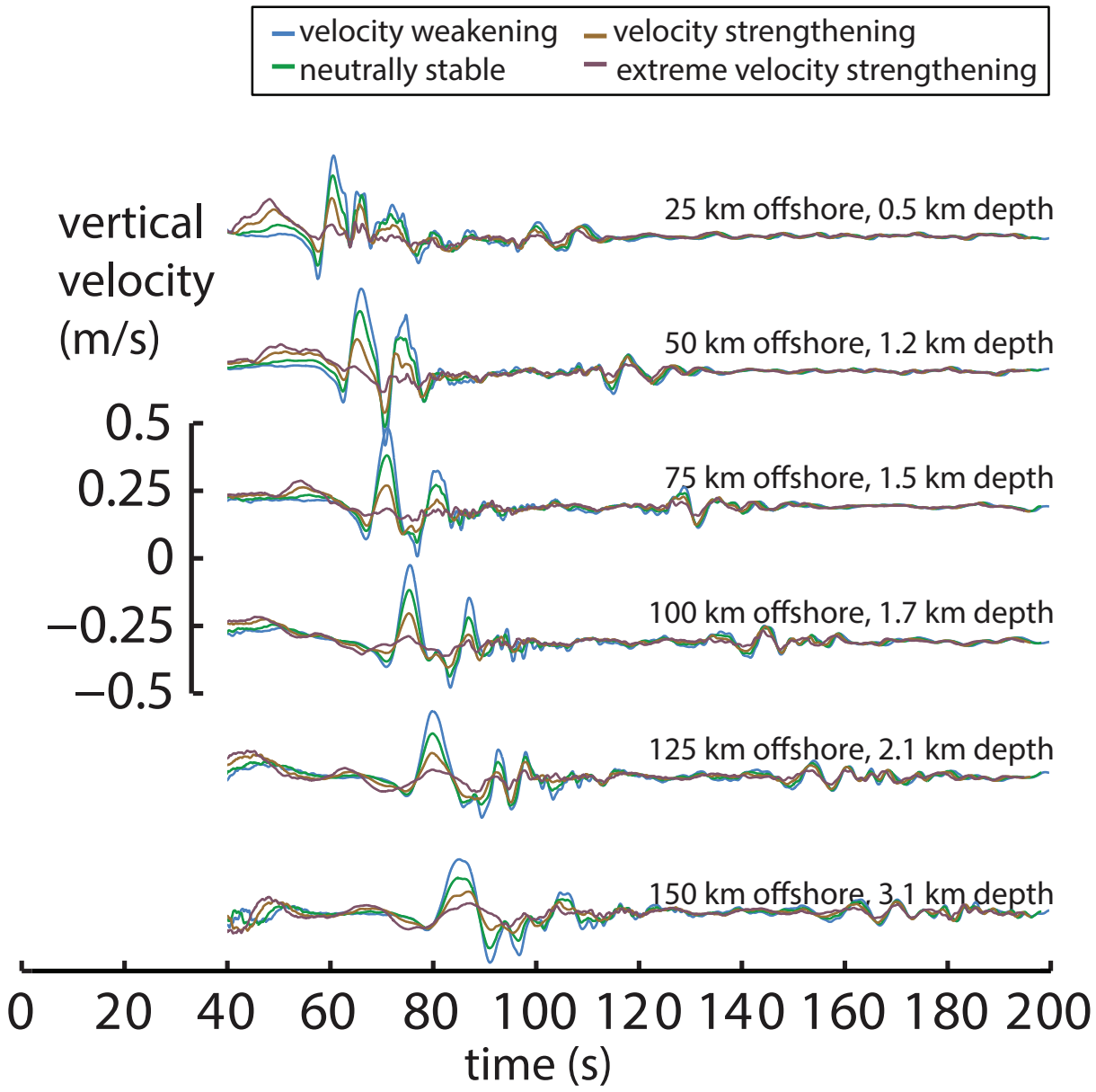

Fig. S6. Synthetic seismograms at seafloor stations landward of trench. Vertical particle velocities in the solid Earth on the ocean bottom, landward of the trench.

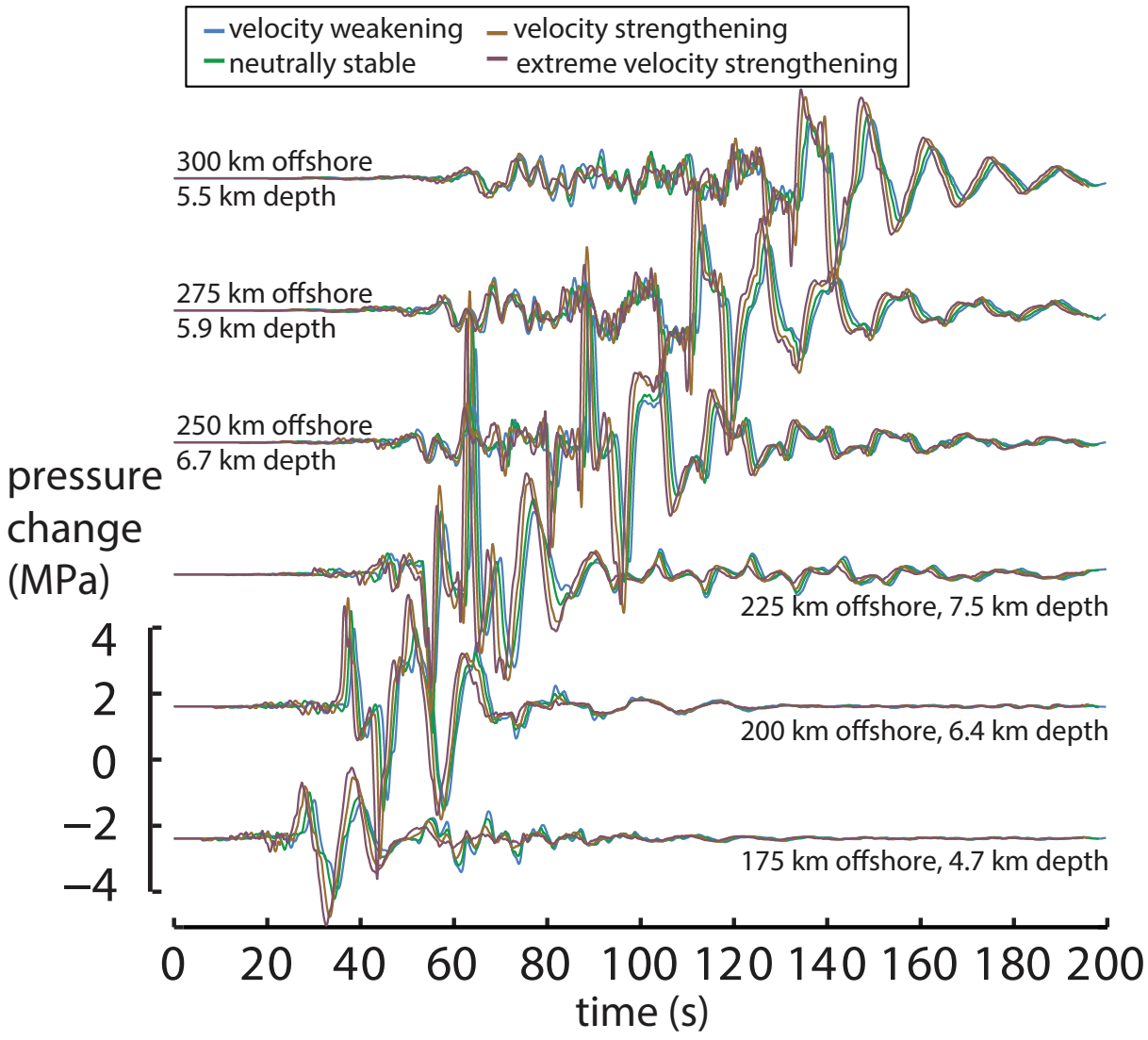

Fig. S7. Pressure changes at seafloor stations farther offshore. Acoustic pressure perturbations on the ocean bottom, farther offshore.

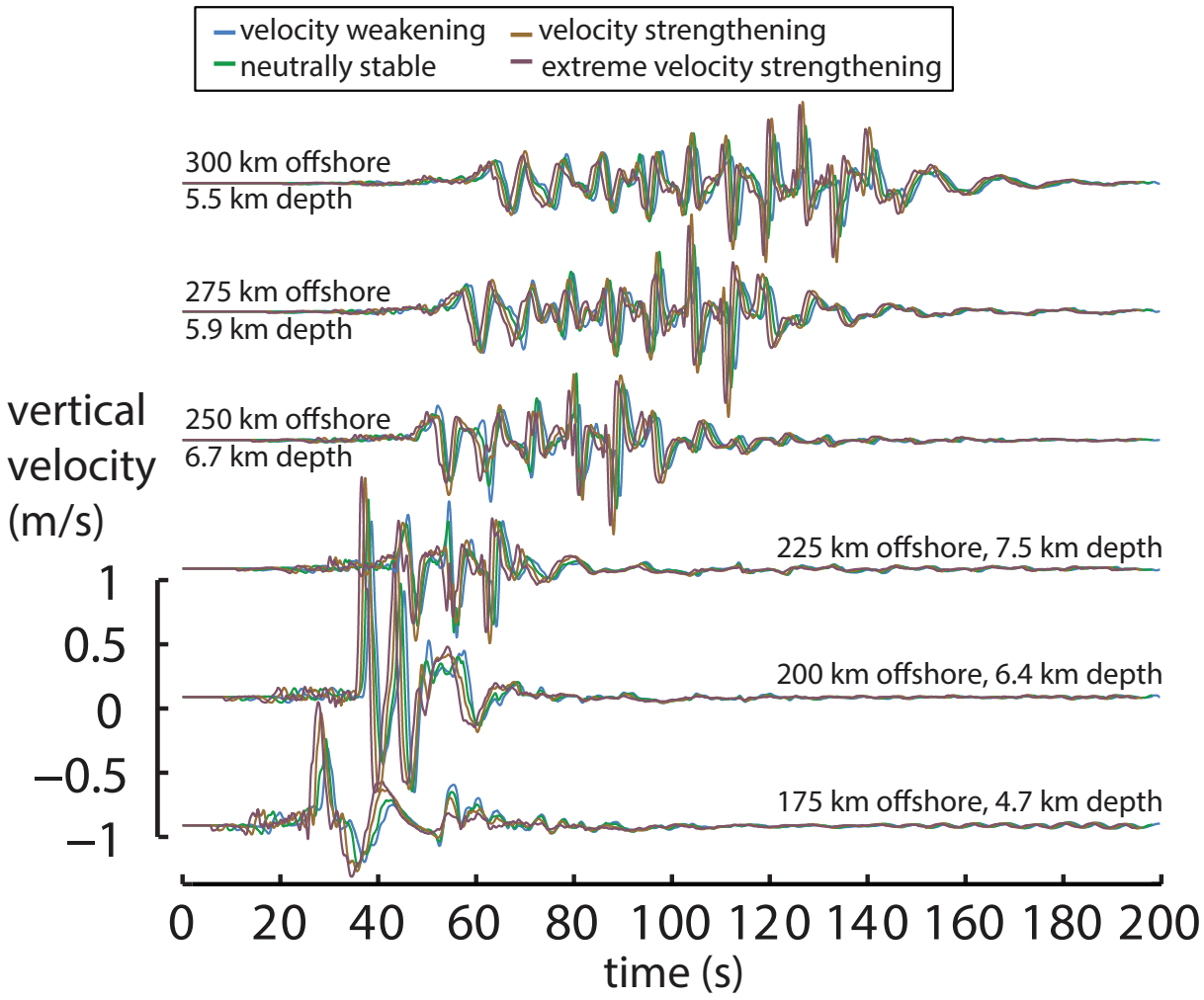

Fig. S8. Synthetic seismograms at seafloor stations farther offshore. Vertical particle velocities in the solid Earth on the ocean bottom, farther offshore.

Movie S1. Seismic and acoustic wavefield from 2011 Tohoku-Oki dynamic rupture simulation. Excitation of seismic and acoustic waves illustrated with vertical particle velocity in the solid Earth and acoustic pressure perturbation in the ocean. The ocean is shifted upward to show seafloor displacement (arrows).